Effect of secondary orientation on notch-tip plasticity in superalloy single crystals

P.A. Sabnis [a], M. Mazière [a], S. Forest [a], Nagaraj K. Arakere [b,*], F. Ebrahimi [c]

[a] MINES ParisTech, Centre des Matériaux, CNRS UMR 7633, BP 87, 91003 Evry Cedex, France
[b] Mechanical and Aerospace Engineering, University of Florida, Gainesville, FL, USA
[c] Materials Science and Engineering, University of Florida, Gainesville, FL, USA

ARTICLE INFO

ABSTRACT

Numerical and experimental evolutions of slip fields in notched Ni-Base Single Crystal superalloy tensile specimens are presented as a function of secondary crystallographic orientation. The numerical predictions based on three-dimensional anisotropic elasticity and crystal plasticity are compared with experimental observations. The results illustrate the strong dependence of the slip patterns and the plastic zone size and shape on the secondary orientation of notches, which can have important consequences on crack initiation. Specific orientations or non-symmetric notch geometries lead to non-symmetric patterns on both sides of the sample. The computations show that strongly different plastic zones are expected in the core of the sample and at free surfaces. The ability of the anisotropic elastic model to anticipate the plastic domains, based on identifying dominant slip systems, is confirmed by the crystal plasticity computations, at low load levels. An important observation is that kink shear banding is a real deformation mode operating at crack tips and notches in high strength nickel-based single crystal superalloys for specific orientations.

1. Introduction

The thermodynamic efficiency of a gas turbine engine increases with higher turbine inlet temperature (TIT) and thus translates to reduced fuel consumption, reduced pollution and lower operating costs. However, many gas turbine engines operate with a TIT in excess of 1000 °C. Such extreme operating environments impose difficult constraints on the choice of materials used in gas turbines. Consequently, Ni-Base Single Crystal (NBSX) super-alloy blades are being used increasingly in turbine engines due to their superior thermal resistance, thermomechanical fatigue, creep, stress rupture and melt resistance capabilities over their polycrystalline counterparts. Directional solidification is used to produce a single crystal blade (Versnyder and Guard, 1960; Milligan and Antolovich, 1987) with the [0 0 1] low modulus orientation parallel to the growth direction. The secondary normal to the growth direction, which is typically referenced to a line parallel to the blade attachment, is random and a grain selector is used to form a single crystal. In most cases, grain selectors are used to produce the desired [0 0 1] growth direction in blade castings. Therefore, the secondary orientations of the single crystal components are determined but not controlled, and hence every blade has a different secondary orientation that can vary from 0° to 90°. Initially, control of the secondary orientation was not considered necessary (Gell and Duhl, 1986). However, recent reviews of the turbine blade lifetime data have indicated that secondary orientation has a significant impact on high cycle fatigue resistance (Arakere and Swanson, 2001, 2002; Arakere et al., 2005). Single crystal turbine blades have complex internal passages

---

* Corresponding author.
E-mail address: nagaraj@ufl.edu (N.K. Arakere).

for forced convection air cooling. The air escapes through an intricate network of cooling holes on the blade surface. Fatigue cracks typically nucleate at the blade leading edge cooling hole locations, due to a combination of mechanical and thermal and cyclic stresses and strains. There is considerable blade-to-blade secondary orientation variation. Finite element simulations of turbine blade responses were performed in (Hou et al., 2008) to illustrate the effect of deviation of ideal [0 0 1] orientation of the blade axis and of the secondary orientation on fatigue life.

Crystallographic fatigue crack nucleation is influenced by the resolved shear stress (RSS) on the slip plane and the normal stress on the slip plane with the highest RSS (Nalla et al., 2002). Persistent slip band (PSB) formation and accumulated slip are also thought to be important for fatigue crack nucleation (Deluca and Annis, 1995; Dunne et al., 2007). Understanding the localisation and the evolution of plasticity in the notches, for a fixed [0 0 1] primary (load) orientation while the secondary (notch) orientation is varied, is important to characterise crack nucleation in the blade cooling holes as a function of blade secondary crystallographic orientation.

Analytical, numerical (two-dimensional) and experimental investigations of slip fields and plastic zones near cracks and notch tips in FCC crystals have been performed by a number of researchers (Rice, 1987; Rice and Saeedvafa, 1988; Saedvafa and Rice, 1989; Shield and Kim, 1994; Shield, 1996; Schulson and Xu, 1997; Drugan, 2001; Crone and Shield, 2001; Crone et al., 2004). The two-dimensional simulations by Rice et al. (1990), Cuitiño and Ortiz (1992) and Mohan et al. (1992) support earlier asymptotic analyses. Three-dimensional (3D) FE simulations are necessary for determining the stress and strain fields on the free surfaces and near notched tensile specimens and fracture mechanics specimens. The first 3D FE simulation of crack tip fields in single crystals was carried out by Cuitiño and Ortiz (1992) and highlights the triaxial nature of the stress and strain fields near the crack tip. Magnan (2002), Siddiqui (2006) and Arakere et al. (2009) have presented a 3D investigation of evolution of plasticity in FCC superalloy single crystal notched tensile specimens based on 3D elastic anisotropic FE model and identified the activated slip systems using the concept of dominant slip system defined as the single slip system that experiences the highest RSS at a given point near the notch. However, the elastic model used is not capable of accounting for nonlinear effects such as latent hardening and lattice rotation afforded by finite strain crystal plasticity simulations. Flouriot et al. (2003) present comprehensive results from 3D crystal-plasticity based finite element simulation of crack tip fields in a compact tension (CT) fracture mechanics specimen and show that there are strong differences between the crack tip plastic strain fields observed at the free surface and mid-section of the CT specimen tested. Mapping of lattice rotation on the free surface in the crack tip zone was also performed using EBSD mapping. These observations revealed the existence of intense slip bands and also kink bands emanating from the crack tip, which was also observed by Kysar and Briant (2002) and Patil et al. (2009), for deformation at low temperature and for specific crystal orientations, as essentially predicted by Rice. Kysar et al. (2007) have studied through-thickness variation of crystal lattice rotation induced by wedge indentation in FCC copper and aluminium single crystals. A series of papers by Kysar et al. (2005), Gan et al. (2006), and Borg et al. (2008) have reported detailed analytical (anisotropic slip line theory), numerical (finite deformation strain gradient crystal plasticity simulations) and experimental work, respectively, on the effect of cylindrical voids, their size, and distribution on stress and strain fields and void growth in FCC single crystals. The slip field is shown to exhibit angular sectors around the void circumference. Lattice rotation discontinuities are seen at boundaries between regions of single slip around the void. Slip field sector boundaries observed near the notch in this work show similar features. More recent experimental and numerical analyses of slip system activation in single crystal superalloy fracture mechanics specimens include Aluminium edge notched specimens studies in Patil et al. (2008a, 2008b). Extensions of Rice's initial analysis of the crack tip field are proposed in Patil et al. (2008a, 2008b), and in the review article by Narasimhan et al. (2009). A multiscale modelling using molecular dynamics simulations to bridge across nano, micro and meso scales is employed to predict work hardening in FCC aluminium single crystals by Groh et al. (2009). A novel yield function representing the overall plastic deformation in a single crystal has been presented recently based on the principle of maximum dissipation where single crystal plasticity is considered as a constrained optimisation problem in which constraints are yield functions for slip systems (Zamiri and Pourboghrat, 2010). Horstemeyer and Bammann (2010) present a comprehensive review of internal state variable theory for inelasticity that covers a wide range of applications in multiscale modelling of materials and design optimisation. Such models implemented into a finite element code are useful for simulating large scale deformation in polycrystalline materials. Rossiter et al. (2010) present a new crystal plasticity scheme with explicit time integration scheme implemented into a finite element code that is capable of utilising EBSD data for crystal orientation and is suitable for large-scale 3D simulation of polycrystalline microstructures.

There exist numerous studies in the literature that show that crystal plasticity is able to capture the strain and lattice orientation fields in large grains or even single crystals for copper and aluminium for instance. However, results for slip activity in significantly stronger metals like NBSX do not exist for notched specimens, to our knowledge. Such a validation is of the utmost importance for engineering applications in turbine blades.

The behaviour of NBSX materials remains almost elastic-ideally plastic until around 600–700 °C, after which elastic–visco-plastic behaviour is observed. The information obtained from tests at room temperature is relevant over a large range of in-service temperature conditions for which strain localisation in the form of intense slip bands can be observed. As such phenomena are known to play a significant role in the initiation of fatigue cracks, the ability of crystal plasticity simulations to accurately capture such phenomena needs to be tested and validated. Keeping these reasons in mind, the work in the following article has been carried out at room temperature.

We present fully 3D crystal plasticity finite element analysis (CPFEA) of the stress–strain fields near the notch tip in double-notched NBSX tensile specimens for three different orientations. The primary orientation is fixed along the [0 0 1]
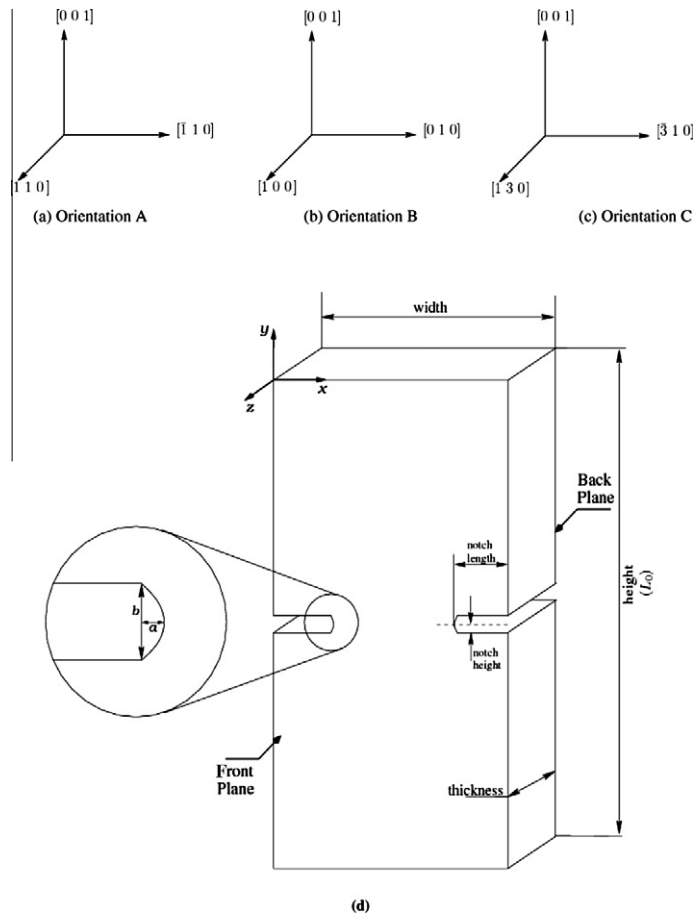
Fig. 1. (a)–(c) Orientations tested. (d) Geometry definition of the specimen.

direction while the notch directions are parallel to $[\bar{1}10]/[1\bar{1}0]$, $[010]/[0\bar{1}0]$, and $[\bar{3}10]/[3\bar{1}0]$ for the three orientations investigated, shown in Fig. 1(a)–(c). The specimen geometry definition is shown in Fig. 1(d) and the dimensions of the specimens used in experiments are provided in Table 2. The CPFEA model incorporates effects of hardening and lattice rotation. Experimental results on notched tensile tests at room temperature are then compared with numerical simulations in terms of slip line distributions. Section 2 describes the experimental and material procedures and the development of slip traces near the notches recorded using optical microscopy for the two orientations studied. Section 3 describes the CPFEA model and the computational tools implemented for the numerical study. Section 4 is devoted to numerical results and the

Table 1
Definition of slip systems used in the crystal plasticity model.

Slip system number	Normal to slip plane	Slip direction
1	(111)	$[\bar{1}01]$
2	(111)	$[0\bar{1}1]$
3	(111)	$[\bar{1}10]$
4	$(1\bar{1}1)$	$[\bar{1}01]$
5	$(1\bar{1}1)$	$[011]$
6	$(1\bar{1}1)$	$[110]$
7	$(\bar{1}11)$	$[0\bar{1}1]$
8	$(\bar{1}11)$	$[110]$
9	$(\bar{1}11)$	$[101]$
10	$(11\bar{1})$	$[\bar{1}10]$
11	$(11\bar{1})$	$[101]$
12	$(11\bar{1})$	$[011]$

Table 2
Dimensions of the specimens used in the computation. All dimensions are in mm and correspond to the actual dimensions of the experimental specimens (Arakere et al., 2009).

Dimension	Orientation A	Orientation B	Orientation C
Width	5.100	5.040	5.100
Height	19.000	17.594	19.000
Thickness	1.800	1.820	1.770
Right notch length	1.300	1.394	1.400
Left notch length	1.550	1.360	1.390
Right notch height	0.113	0.084	0.085
Left notch height	0.111	0.084	0.086
a (for both notches)	0.055	0.056	0.055
b (for both notches)	0.226	0.168	0.172

comparison with experimental data. Section 5 presents a brief discussion of the results and a comparison of CPFEA and Anisotropic Elasticity (AE) simulations. Section 6 then presents the conclusions of the following study.

2. Experimental results

2.1. Material and experimental procedure

PWA 1480 single crystal Ni-base superalloy castings in the form of two 25 mm diameter (1 in.) bars with cylinder axis along the [0 0 1] direction were provided in as-heat-treated condition by Pratt and Whitney. The microstructure of the alloys consisted cubical primary γ' precipitates in a matrix of solid solution γ. Both crystals did not have any noticeable eutectic pools or pores. Laue X-ray back-reflection technique was employed to identify the crystallographic orientations of them, based on which the samples' directions were realised. Although this material consists of two phases (FCC γ-matrix and $L1_2$ γ'-precipitate), in the case where particle shearing takes place at room temperature, geometrically, plastic deformation is analogous to a single-phase FCC crystal. The γ' precipitate is an intermetallic. Consequently, these materials have a critical resolved shear stress (CRSS) that is an order of magnitude higher than pure Cu or Al. The advantage of using a superalloy crystal is that it yields at considerably high applied stresses and therefore the applied load levels at small plastic zones can be accurately controlled and measured. Fig. 1 presents the geometry of the double-notched tensile specimens used in this study, the dimensions of the test specimens are provided in Table 2. Front and back planes of the specimen are identified separately in Fig. 1 to facilitate the discussion of slip fields for specimens with an asymmetrical orientation. Electro-discharge machining (EDM) technique was employed to prepare dog-bone shaped un-notched samples. Then they were carefully polished on both faces and sides to remove any damage caused by EDM. Three sample orientations with notches parallel to the $[\bar{1}10]/[1\bar{1}0]$ (orientation A) and $[010]/[0\bar{1}0]$ (orientation B) and $[\bar{3}10]/[3\bar{1}0]$ (orientation C) directions were prepared (see Fig. 1). Prior to the introduction of notched, X-ray analysis confirmed that all expected orientations were off by no more than 8°. It should be pointed out that the [0 0 1] primary orientation direction in turbine blade castings is also
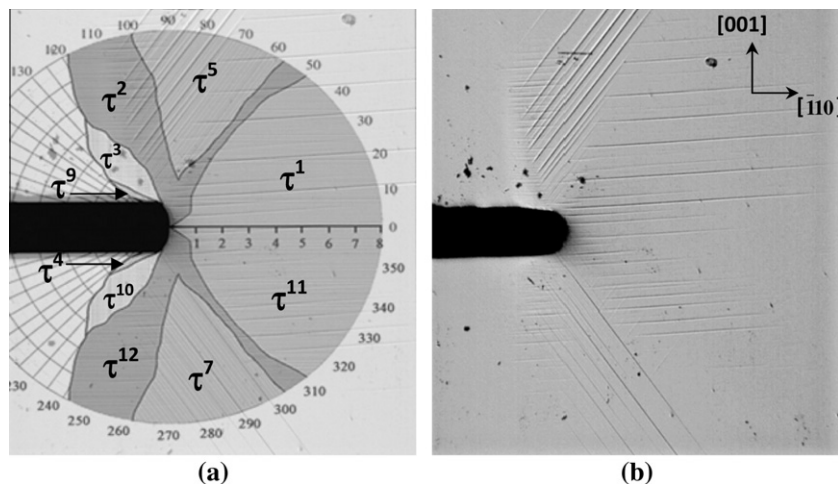

Fig. 2. Comparison of experimentally observed slip fields near the notch for orientation A at a load of 4982 N with numerical results. (a) Numerical shear stress fields generated by anisotropic elasticity simulations superposed on to the experimentally observed slip lines. (b) Experimentally observed slip lines on the specimen (see Table 2 for specimen dimensions).
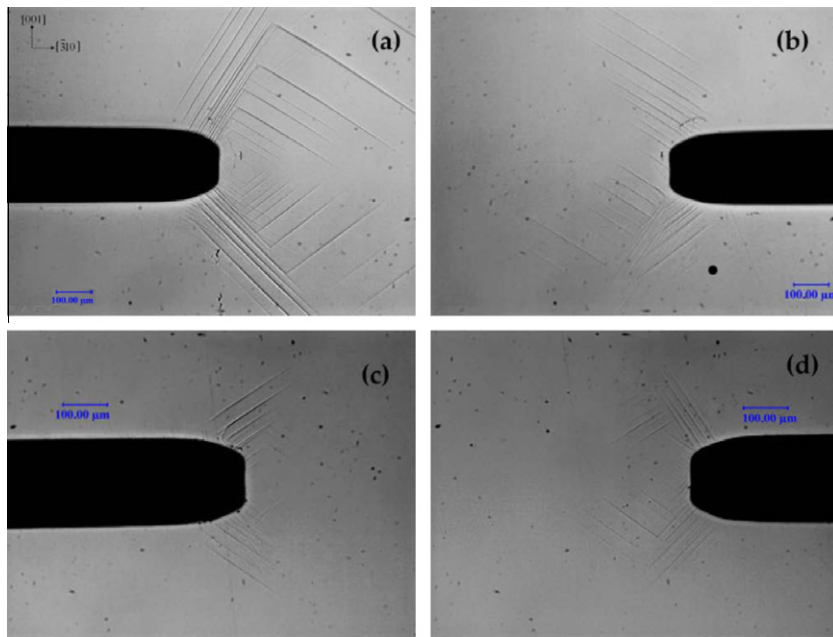
Fig. 3. Slip fields observed at the specimen surface for orientation C at 3500 N load ($K_I = 30$ MPa $\sqrt{M}$, see Table 2 for specimen dimensions). (a) Front plane, left notch. (b) Front plane, right notch. (c) Back plane, right notch. (d) Back plane, left notch.

controlled to within 8–10°. The notches were introduced using a slow speed saw with a thin diamond blade. A special fixture was designed to achieve co-planar notches with approximately equal lengths on both sides. Consistent notch tips were produced with careful and methodical procedures. The dimensions of the specimens used in the experiments are presented in Table 2.

The yield stress for the considered single crystal superalloy was evaluated by conducting tensile tests along the [0 0 1] direction using dog-bone samples with rectangular cross sections. The analysis of deformation bands on the face and the sides of the samples revealed that slip took place along the {1 1 1} planes (Ebrahimi et al., 2006; Westbrook, 2005; Ebrahimi and Westbrooke, 2008). Assuming the activation of octahedral slip systems, the average critical resolved shear stress (CRSS) value was measured to be 324 MPa. We note that this CRSS value is more than 30 times higher than that of pure Aluminium. In order to investigate the evolution of plasticity near notch tips, samples were loaded to various levels of apparent stress intensity factors (i.e. calculated based on the sharp crack isotropic assumption) in the range of $K_I = 20$ MPa $\sqrt{m}$ to 50 MPa $\sqrt{m}$. The development of slip traces near the notches was recorded using optical microscopy.

2.2. Slip field development for orientation A

The experimentally observed slip bands around the notch for orientation A, at a load level of 4982 N ($K_I = 50$ MPa $\sqrt{m}$), are shown in Fig. 2(b). The slip bands show a slight asymmetry about the notch axis, which can be attributed to the crystallographic deviation from the [0 0 1] orientations as well as any minor misalignment in the loading fixture. Fig. 2(a) shows the comparison of experimentally observed slip bands with numerical RSS fields generated by anisotropic elastic simulations.

2.3. Slip field development for orientation B

The slip fields activated at the surface for this orientation are very different from those observed for orientation A. At a lower load of 1780 N ($K_I = 20$ MPa $\sqrt{m}$), slip traces along [0 1 $\bar{1}$] direction are activated, corresponding to the (1 1 1) or ($\bar{1}$ 1 1) slip planes. At the higher load of 3456 N ($K_I = 45$ MPa $\sqrt{m}$), a second set of slip systems becomes activated at a larger distance from the notch tip, with slip traces along the [0 1 1] direction, corresponding to (1 1 $\bar{1}$) or (1 $\bar{1}$ 1) slip planes.

2.4. Slip field development for orientation C

Optically observed slip bands around the notch for orientation C, for the front plane of left and right notches are shown in Fig. 3. The "left" and "right" notch designations are based on looking at the front face. This orientation has mirror symmetry with respect to the notch plane, i.e. (0 0 1) plane, and hence it exhibits symmetrical plastic zone on top and bottom half of

Table 3
Main characteristics of the used finite element meshes (DOF: degrees of freedom which are the nodal displacement components).

Orientation	Total number of elements in mesh	Number of elements along the thickness	Number of DOFs
A	24,030	10	320,484
B	20,690	10	276,660
C	26,940	10	358,725

the specimen. However, the crystallographic orientations around left and right notches are different and therefore the plastic zones in their vicinity are anticipated to be different.

Fig. 3 presents experimental slip fields at the left and right notches for orientation C, at a load level of 3500 N, corresponding to $K_I = 30$ MPa $\sqrt{m}$. Note that the plastic zone sizes observed for the notches at the front and back planes are different due to crystal asymmetry.

3. Crystal plasticity finite element model and computational tools

3.1. Finite element mesh

The computational modelling of the geometry was carried out using the actual dimensions of the specimens from the experiments, presented in Table 2. The specimen was meshed using 10 layers (along the specimen thickness) of 3D quadratic 20-node brick elements. In the meshing of the specimen, regular mesh domains were used in the vicinity of the notch tips (up to a distance of 450 μm from the notch tips). In regions away from the notch tips, free meshing was used.

Two mesh densities were tested initially. The coarse mesh with 16 nodes along the notch tip yielded plastic slip domain boundaries very similar to the finer mesh with 20 nodes along the notch tip. While the finer mesh gives a better resolution of the boundary of the plastic slip domains, the coarser mesh has been retained in the following simulations as a compromise between computation time and a sufficient description of the slip zones for comparison with experimental results.

Since the meshes are tailored to each specimen, there are slight differences in the meshes. Some specific details about each FE mesh in Table 3. In Fig. 1 we have defined the coordinate system (x, y, z) attached to the sample and on the left, the crystal frames associated with the three considered orientations. We call z the axis normal to the front and back free surfaces of the notched specimens.

3.2. Constitutive modelling and material parameters

3.2.1. Crystal plasticity theory

A generalised formulation for crystal plasticity was suggested by Mandel (1973). This formulation uses the multiplicative split of the deformation gradient tensor F, into elastic and plastic parts (E and P) respectively. The decomposition of the deformation gradient is based on the introduction of an intermediate isoclinic configuration having the same crystal orientation as in the initial configuration.

The elastic deformation $\underset{\sim}{E}$ accounts then for the lattice distortion and rotation

$$\underset{\sim}{\mathbf{F}}(\underline{\mathbf{X}}) = \underset{\sim}{1} + \frac{\partial \underline{u}}{\partial \underline{\mathbf{X}}} = \underset{\sim}{\mathbf{E}}(\underline{\mathbf{X}}) \cdot \underset{\sim}{\mathbf{P}}(\underline{\mathbf{X}}) \tag{1}$$

The polar decomposition of the elastic and plastic parts are given as

$$\underset{\sim}{\mathbf{E}} = \underset{\sim}{\mathbf{R}}^e \cdot \underset{\sim}{\mathbf{U}}^e, \quad \underset{\sim}{\mathbf{P}} = \underset{\sim}{\mathbf{R}}^p \cdot \underset{\sim}{\mathbf{U}}^p \tag{2}$$

The lattice distortion and the plastic distortion are given by

$$\underset{\sim}{\mathbf{U}}^e = \underset{\sim}{1} + \underset{\sim}{\varepsilon}^e \tag{3}$$

$$\underset{\sim}{\mathbf{U}}^p = \underset{\sim}{1} + \underset{\sim}{\varepsilon}^p \tag{4}$$

For metals, the elastic strain ε^e remains so small that the rotation matrix R^e essentially gives the lattice rotation under deformation. When the plastic strain ε^p is also small, the previous decomposition provides the usual additive decomposition of the total strain into:

$$\underset{\sim}{\varepsilon} = \underset{\sim}{\varepsilon}^e + \underset{\sim}{\varepsilon}^p \tag{5}$$

where ε is the symmetric part of $F - 1$. A more complete description of the decomposition can be found in Teodosiu (1997). The elasticity state law is

$$\underset{\sim}{\mathbf{\Pi}}^e = J_e \underset{\sim}{\mathbf{E}}^{-1} \cdot \underset{\sim}{\boldsymbol{\sigma}} \cdot \underset{\sim}{\mathbf{E}}^{-T} = \underset{\approx}{\mathbf{C}} : (\underset{\sim}{\mathbf{E}}^T \cdot \underset{\sim}{\mathbf{E}} - \underset{\sim}{1})/2 \tag{6}$$

where σ is the Cauchy stress tensor, Π^e is the second Piola–Kirchhoff stress tensor with respect to the intermediate configuration and C is the fourth rank tensor of elastic moduli. The term J_e is the determinant of the elastic deformation ($\det E$).

The evolution of the plastic slip γ^s is controlled by the implementation of the Schmid criterion according to which plastic deformation occurs only after the RSS τ^s exceeds a CRSS value, τ_c. The driving force for plastic slip is the RSS defined as

$$\tau^s = \mathbf{M} : (\underline{m}^s \otimes \underline{n}^s) \tag{7}$$

where

$$\mathbf{M} = J_e \mathbf{E}^T \cdot \sigma \cdot \mathbf{E}^{-T} \tag{8}$$

and $\underline{m}^s$ and $\underline{n}^s$ are the slip direction and the slip plane normal respectively and M is the Mandel stress tensor. The slip rate is computed by means of a viscoplastic flow rule:

$$\dot{\gamma}^s = \left\langle \frac{|\tau^s| - \tau_c}{K} \right\rangle^n \operatorname{sign}(T^s) \tag{9}$$

In the latter equation, the power law is such that large values of n and low values of K account for an rate-independent plastic behaviour in the usual range of strain rates.

In the simulations presented here, linear isotropic hardening is included and the interaction between slip systems is ignored, as recognised by Nouailhas et al. (1995) for Ni-base superalloys:

$$\tau_c = R_0 + Hv^s \tag{10}$$

where

$$\dot{v}^s = |\dot{\gamma}^s| \tag{11}$$

and R_0 is the initial CRSS and H is the hardening modulus.

3.2.2. Parameter identification and loading curves

The material parameters are calibrated using the tensile curve for a smooth specimen. The curve used for the calibration is shown in Fig. 4. It displays a typical feature of the mechanical behaviour of NBSX materials at low temperature, namely a high yield stress with a plateau corresponding to the propagation of slip bands filling the gauge length, followed by slight hardening. We have chosen to represent this behaviour by an elastic-quasi-ideally-plastic behaviour with a slight linear hardening component. The parameters used for the simulations are given in Table 4. The table also includes the cubic elasticity moduli used. The main parameter is the initial CRSS, $R_0 = \tau_c = 324$ MPa. A small linear hardening component is introduced to limit the strain localisation phenomena in perfect plasticity. Viscosity parameters are used only for the selection of slip systems. Their values are such that the material response is practically strain rate independent in the range of strain rates involved in the tests. It does not reflect the plateau stress observed in tension on the smooth specimens even though models for simulating the propagation of slip bands do exist Forest (1997). However, we do not think this phenomenon to be essential for the material response in the presence of notches.
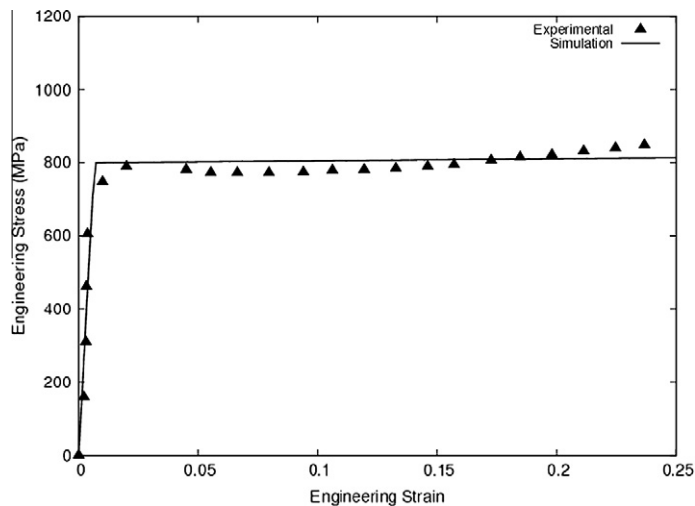

Fig. 4. Tensile stress–strain curve of a smooth specimen along direction [0 0 1] used for identification of the material parameters.

Table 4
Parameters used in the CPFEA simulations.

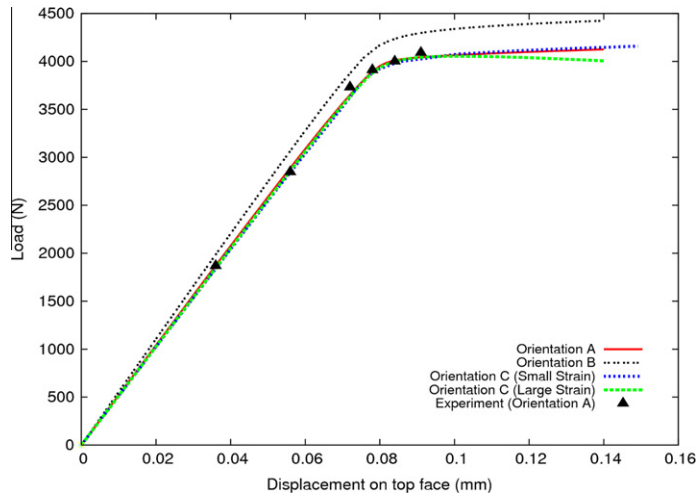| Parameter	Value
Elastic moduli (MPa)	
y1111	250,000
y1122	163,000
y1212	129,000
Flow rule parameters	
K	4 MPa s$^{1/n}$
n	15
Linear isotropic hardening parameters	
H	75 MPa
R_0	324 MPa

Fig. 5. Load vs. displacement curves of compact tension of notched specimens. The displacement is imposed on the top face of the specimen (face normal to the y-axis in Fig. 1). The triangles represent the experimental observations for orientation A.

The curves shown in Fig. 5 are the load–displacement curves for the notched specimens subject to tension loading. The triangles in Fig. 5 represent the experimental data points obtained for the specimen of orientation A. The tensile loading is imposed on the top face of the specimens while keeping the bottom face rigid. The loads are measured along the top face of the specimen and hence the curves indicate global loading curves. Thus, the curves shown in Fig. 5 do not reflect the stresses experienced by the specimen locally at the notch tip. Due to the fact that the loading direction is [0 0 1] for all three specimens, the loading curves are still very close. Strong differences will be observed at the local level close to the notches. Some of the differences also stem from the slight differences in the geometry of the specimens as shown in Table 2.

3.3. Post-processing procedures

The FE simulations provide the discretised fields of stress, strain, amounts of plastic slip γ^s and RSS τ^s for all slip systems. The results presented in this work show the maps of the dominant activated slip systems around the notch tips. The post-processing procedures used in the preparation of these maps are described below.

As a first step, the absolute values of the plastic slips at a given time step were computed at each integration point in the finite element mesh. The maximum among these values and the corresponding slip system number $1 \leqslant n_{max} \leqslant 12$ were stored. This field of n_{max}, can be plotted as a contour plot; these maps will henceforth be referred to as γ-maps. The scale used in the γ-maps is shown in Fig. 6, unless indicated otherwise. Each number on the scale indicates the corresponding slip
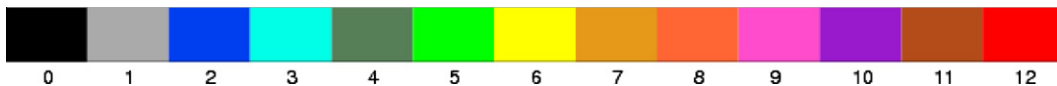

Fig. 6. Scale used for the dominant plastic slip maps (γ-maps). Each number corresponds to the respective slip system number as defined in Table 1. The number 0 indicates no plastic slip.

system as defined in Table 1. When, for symmetry reasons, several slip systems take the same highest slip value, the largest system number is retained for n_{max} and a negative sign is attached to this index, as a convention. The value of $n_{max} = 0$ is attributed to material points undergoing purely elastic deformation. For the post-processing procedures, the slip system is considered to be inactive when the absolute value of the plastic slip of that particular system is smaller than 10^{-7}. This value is arbitrarily selected, but is essential in differentiating the regions of the specimen undergoing purely elastic deformation from the regions exhibiting plastic slip.

For comparison of the experimental results and the crystal plasticity simulations, the γ-maps were superimposed onto the experimental optical photographs. The visible slip lines were then compared to the contours indicated by the γ-map. Comparisons of the γ-maps and the RSS contour maps computed from purely elastic computations from literature are also presented.

3.4. Testing of the γ-maps generated

To ensure that the post-processing procedure described above is able to handle cases of symmetry where two or more active slip systems attain identical highest slip values, the following tests were simulated.

A single crystal specimen similar to the double notched specimens described in the earlier sections, but with idealised dimensions (to ensure symmetry of the specimen geometry) was modelled in 2D and 3D. The 2D model was a quarter piece symmetric model. The completely symmetric orientation B was used in these tests as it was expected to be the candidate most likely to exhibit the behaviour being investigated in this section (viz. multiple dominant slip systems). Symmetry boundary conditions were imposed and a monotonic tensile load was applied. Application of the post-processing procedure to the results of the 2D simulations indicated multiple dominant slip systems (indicated by a negative index on the contour plot).

The 2D model was then extruded to form a one-eighth symmetric 3D model of the same specimen. Symmetry boundary conditions were imposed on the 3D model and the monotonic tensile load was applied. The application of the post-processing procedure to the results of the 3D computation resulted in unique dominant slip systems. The results of these two tests are shown in Figs. 7 and 8. Fig. 8 also shows the strong changes in the slip fields from the free surface to the core.

The test simulations point at two aspects,

(i) The numerical implementation of the post-processing procedure described in the earlier section is capable of handling cases of multiple dominant slip systems.
(ii) The results indicating unique dominant slip systems in the 3D case originate from free surface and thickness effects. This point will be discussed further in the following sections.

4. Results and comparison

4.1. Prediction of plastic strain field

The evolution of plastic strain in NBSX material and the effect of the secondary orientation on the material's response were studied by means of crystal plasticity simulations. The simulations are used to quantify the differences in the plastic
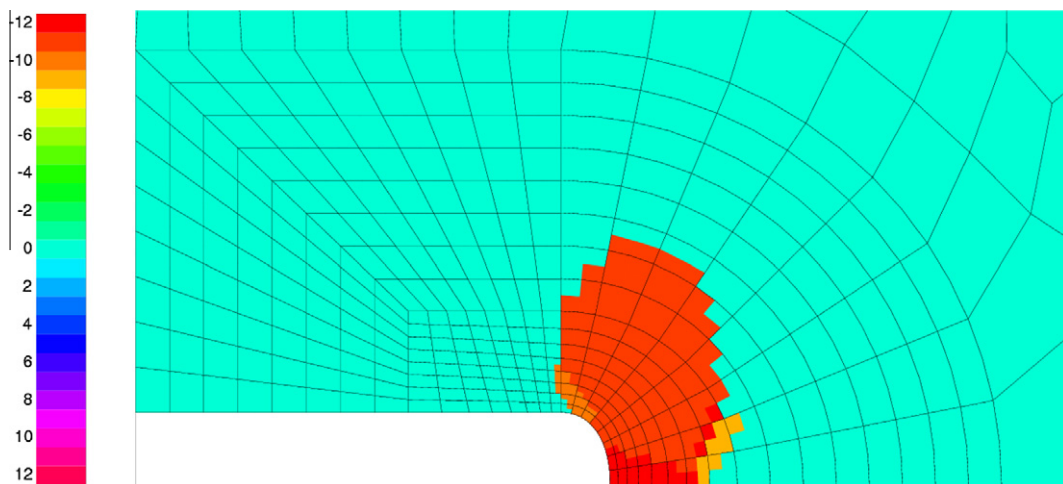

Fig. 7. 2D simulations of a quarter piece symmetric model at an imposed displacement of 03 mm (943 N) on the top edge. Negative slip system numbers denote multiple dominant slip, the highest integer value being kept.
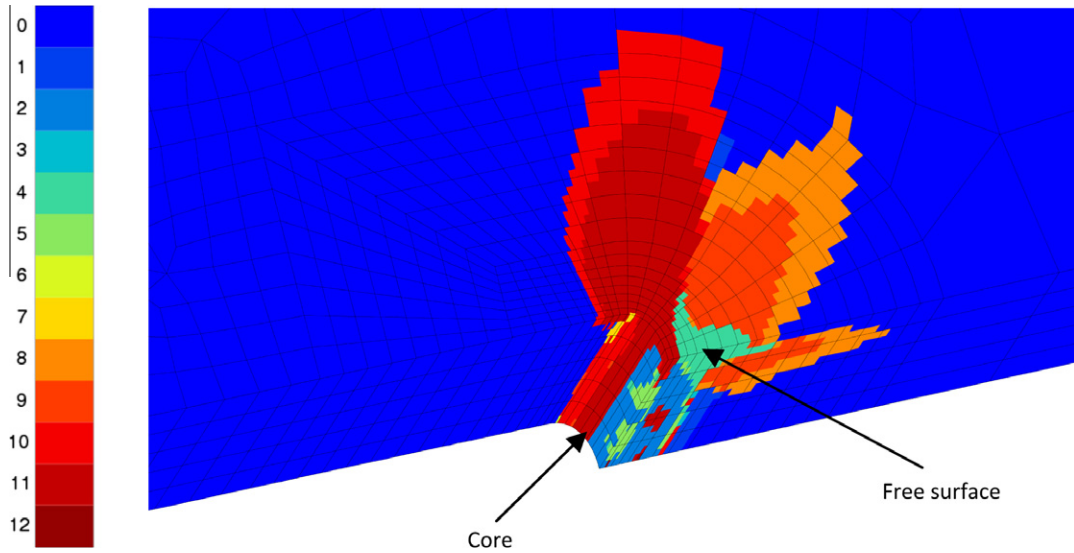
Fig. 8. 3D simulations of a one-eighth piece symmetric model at an imposed displacement of 0.03 mm (819 N) on the top face. A strong change in the plastic slip fields from the free surface to the core is apparent.

strain field at notches depending on the secondary orientation. The plastic strain fields at the free surface for the three orientations are recorded at loads close to 3500 N (3509 N for orientation A, 3510 N for orientation B and 3486 N for orientation C). These loads still correspond to a globally linear response of the sample (see Fig. 5), but confined plasticity has already started at the notches. The equivalent strain is computed using the relation,

$$\varepsilon_{eq} = \sqrt{\frac{2}{3} \varepsilon_{ij}^p \varepsilon_{ij}^p} \tag{12}$$

where the ε_{ij}^p are the plastic strain components at a given time step. It can be observed from the Fig. 9 that the secondary orientation strongly influences the development of plasticity. The plastic zones at the free surfaces exhibit a typical butterfly shape. Plasticity mainly develops at 45° for the three orientations. Significant plasticity is observed at 90° for orientation A. The plastic zone size, defined as the maximum distance from the crack tip at which the equivalent plastic slip becomes less than 0.001, is a strong function of orientation, as evidenced by Fig. 9 which shows the distribution of equivalent plastic strain for orientations A, B and C. The plastic zone size is about 250 μm for orientations B and C for the considered loads of Fig. 9 whereas it is ~450 μm for orientation A at the same load. Due to the absence of a vertical symmetry plane, the left and the right plastic zones are strongly asymmetric for orientation C, in contrast to the orientations A and B.

As already pointed out in Flouriot et al. (2003) for CT specimens, the plasticity in single crystals is a highly 3D phenomenon so that the observation of results at the free surface does not give the complete picture of the deformation processes. In Fig. 10, for illustration we compare the activity of some slip systems at the free surface and along the thickness of the notch. From the Fig. 10, it is observed that at the same load of 3510 N (for orientation B), the slip system numbered 1, 2 and 4 are activated on the surface of the specimen. The slip system 10 however, is not activated on the surface of the specimen, but is active along the notch tip.

It is also observed that the amount of plastic slip due to the slip system number 2 on the surface is very small. However, all the slip systems are active in the core, indicating high amounts of strain localisation along the notch tip of the specimen. Table 5 indicates the activated slip systems on the free surface of the specimens as indicated by CPFEA. The fields of activated plastic slips are then used to determine the dominant slip systems depicted in the next section.

4.2. Dominant slip system maps

The "*dominant slip systems*" defined as those slip systems that experience initially the highest RSS at a given location near the notch coincided with the experimentally observed activated slip systems (Arakere et al., 2009). The plastic strain maps cannot be directly compared to the experimental results since no strain field measurements were performed on these samples. Instead, the γ-maps described above are compared to the observed slip lines.

The experimentally observed slip lines can be associated with traces of the potential {1 1 1} slip planes intersecting with the specimen surface, as shown in Fig. 11 for orientations A, B and C. As a demonstration of the effectiveness of CPFEA predictions, the γ-maps were superimposed on the experimentally observed slip field results for orientations B and C shown in Fig. 12. From the experimental observations alone, it is not possible to identify uniquely the activated slip systems. However, we can compare the slip systems predicted by the CPFEA simulations and identify the activated slip systems among the three
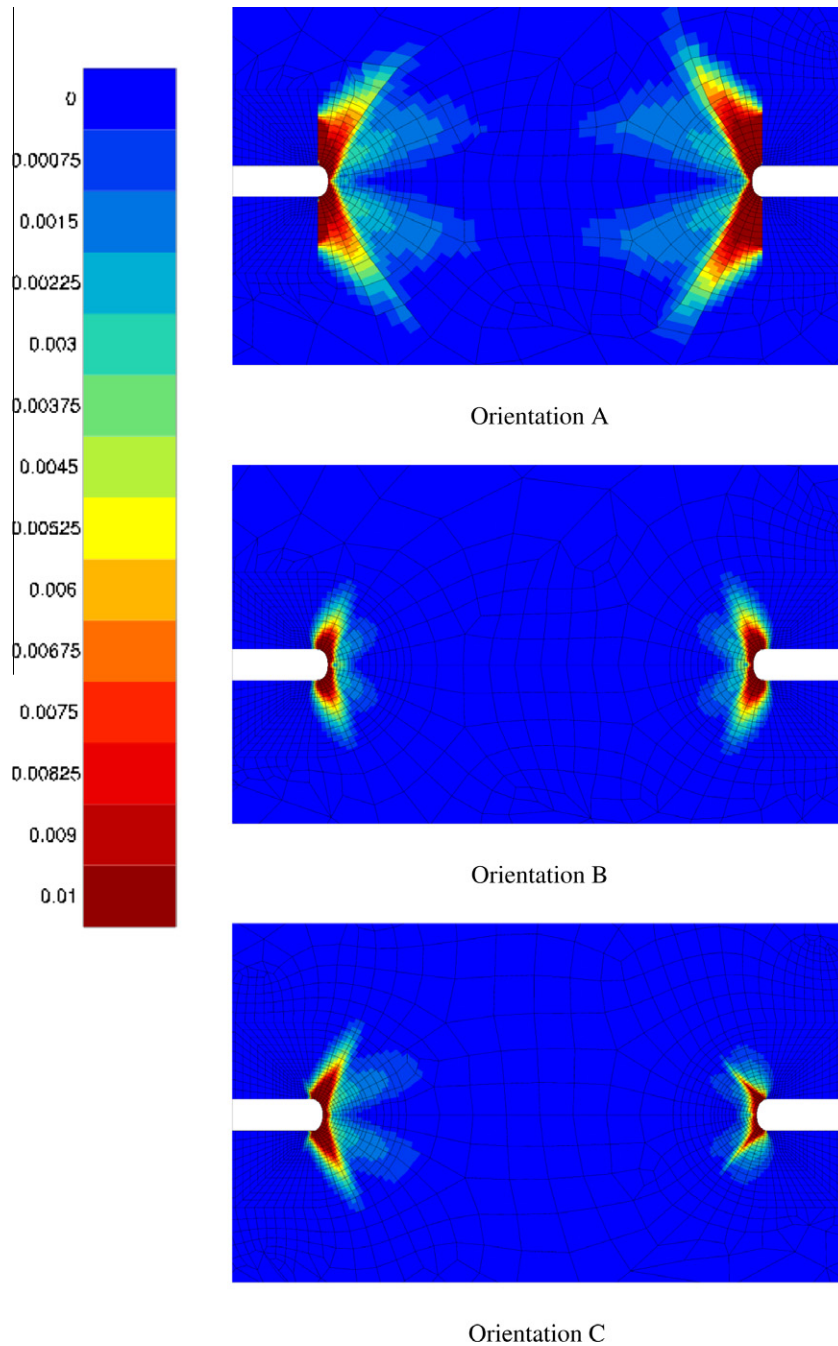
Fig. 9. Equivalent plastic strain maps for the three orientations at a load close to 3500 N (see Table 2 for specimen dimensions).

potential slip systems associated with each slip trace intersecting the surface. Among these potential systems, we can exclude those having a Burgers vector perpendicular to the axis z, since they would not produce a step on the free surface. Such a comparison is drawn in Fig. 12. It shows that in most cases, the activated slip planes are predicted with good accuracy in the proper zones. Indeed, the slip plane corresponding to the predicted dominant slip system (highlighted in Fig. 12) is in good agreement with observed slip lines. An ambiguity arises for orientation B because of the two potentially observable slip plane traces, but there is no such ambiguity for orientation C. Figs. 13 and 14 respectively show the superposition of the predicted γ-maps on the experimentally observed images for orientations B and C, at different load levels. In general, slip lines are contained in the predicted zones and individual slip lines very often end at the boundaries of the dominant slip domains. In some cases, the slip lines cross the boundaries of the predicted domain showing that there are still limitations in
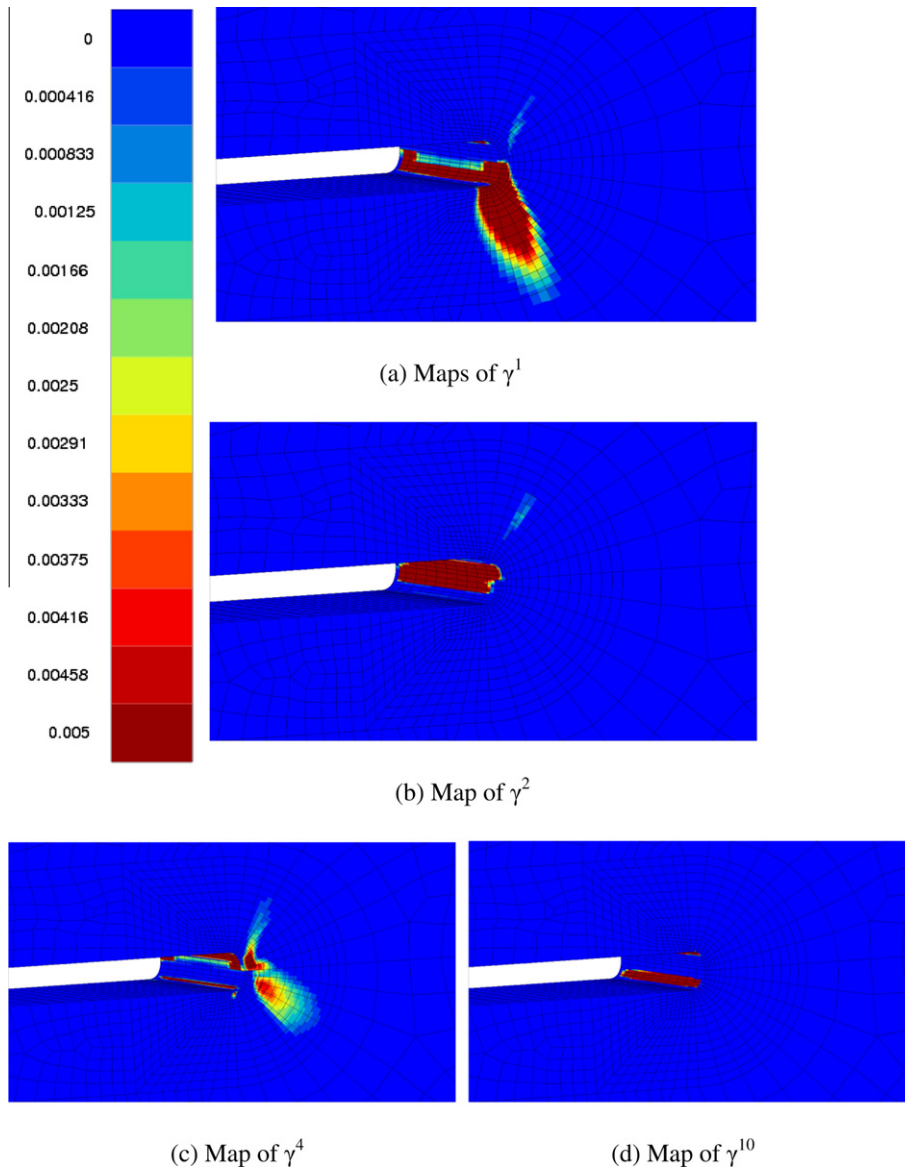
(a) Maps of γ^1

(b) Map of γ^2

(c) Map of γ^4 (d) Map of γ^{10}

Fig. 10. Some individual plastic slip contour maps for orientation B at a load of 3510 N (see Table 2 for specimen dimensions).

Table 5
Activated slip systems on the surfaces of the three orientations as predicted by CPFEA simulations.

Orientation (load at observation)	Activated slip systems on surface(strong activation)	Activated slip systems on surface(weak activation)	Inactive slip systems
A (3509 N)	1, 2, 5, 7, 11, 12	3, 4, 9, 12	6, 8
B (3510 N)	1, 4, 9, 11	2, 5, 7, 12	3, 10
C (3486 N)	1, 2, 5, 7	3, 10	4, 6, 8, 9

the accuracy of the predictions. This is mainly attributed to the slight deviation in the test specimen orientation from the ideal one.

4.3. Core vs. surface behaviour

Numerical vs. experimental comparisons are possible only at free surfaces. However, full 3D computations are needed since the strain field at the free surface and in the core of the specimens can be shown to differ significantly. Fig. 15 shows
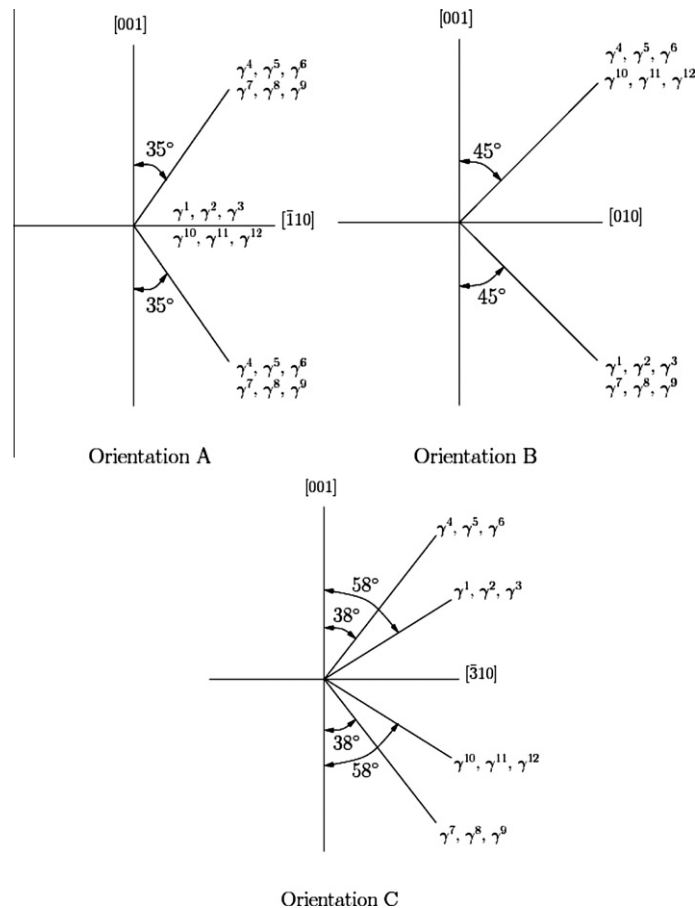
Fig. 11. Theoretically calculated slip traces on the free surfaces. The figure indicates the theoretical angles that are expected to be made by the traces of the slip planes on the surface of the specimen for the three orientations.

the observations in the mid-plane of the specimen (orientation B) as predicted by CPFEA. It is observed that the dominant active slip patterns in the core differ significantly from the dominant active slip patterns observed on the surface. In particular, at this load level, the ligament at the core of the sample has no elastic region left and the entire region has non-zero plastic strains whereas an elastic zone remains in the ligament region on the free surface.

Following this observation, stress state plots were generated for orientation A. The stress state plots were then compared to the plane strain analytical yield surface from the literature (Rice, 1987; Flouriot et al., 2003). These plots are presented in Fig. 17. Fig. 17(a) presents the stress plot for a 2D plane strain simulation. Fig. 17(b) presents the stress state plot at the core of a 3D simulation, whereas the Fig. 17(c) presents the stress state at the free surface of the 3D specimen. The stress state plots are presented at loads corresponding to an imposed displacement of 0.05 mm and 0.07 mm on the top face. This corresponds approximately to loads of 2600 N (globally elastic regime) and 3750 N (globally elastic–plastic transition regime) respectively. The blue lines represent the data set obtained at a distance of 145 μm from the notch tip (blue points in Fig. 16) where as the red lines represent the data set obtained at the notch tip (red points in Fig. 16). It is observed that for the 2D simulation the stress state remains quite close to the analytical yield surface. For the core of the 3D specimen, it is observed that the stress state at the notch tip exceeds to beyond the analytical yield surface, indicating the onset of localised plastic hardening at the notch. The stress state ahead of the notch tip appears to adhere more closely to the analytical yield surface. From the stress state plot in Fig. 17(c), it appears that the stress state plot at the specimen surface is much more complicated than the hexagonal yield surface predicted analytically for the plane strain situation.

For the symmetric orientations A and B, one would expect multiple dominant slip systems in the core which exhibits very high amounts of strain localisation. But, the CPFEA results indicate that there is only one dominant slip system at any given time step even at the core, as discussed earlier. It is to be noted that the post-processing procedures here indicate only the slip system with the highest amount of plastic slip at a time step. This does not necessarily mean that the indicated slip systems in the γ-maps are the only active slip systems at the time step. The secondary active slip systems can also be listed to compare with the experimental results. This is discussed further in Section 5.2.
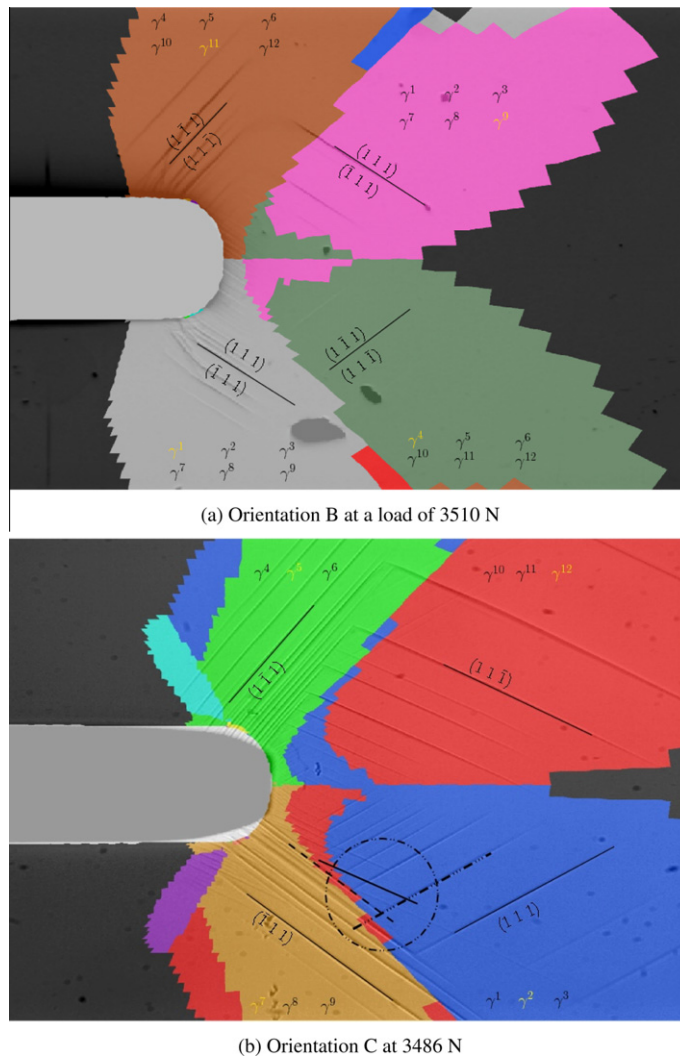
(a) Orientation B at a load of 3510 N

(b) Orientation C at 3486 N

Fig. 12. Analysis of the superimposed images for orientations B and C. The slip planes potentially activated according to the experiment are indicated, together with the corresponding slip systems and the highlighted dominant slip systems from the simulation. The encircled region in (b) shows one of the zones in which multiple slip lines are observed in experiment.

The variations in the dominant slip systems through the thickness can mean that under fatigue loading, the point of crack initiation can be strongly dependent on secondary orientation. Nalla et al. (2002) have indicated that the factors playing an important role in fatigue crack nucleation are the magnitudes of RSS on the slip planes and the normal stress on the slip plane that is initially activated. The variation of activated slip systems through the thickness implies that the load level induces plasticity and its location varies as a function of crystallographic orientation and through thickness location.

4.4. Simulations at finite deformations

The previous results were obtained from the finite element simulations based on the small strain formulation of the single crystal model. It is essential to validate these simulations by comparing them to FE simulations with the finite deformation model described in Section 3.2.

A comparison of the γ-maps obtained from small strain and large strain formulations of the CPFEA simulations indicate that there is no significant difference in the γ-maps generated by the two formulations for the considered load levels. However, the small strain formulation is preferred to the large strain formulation for the problem under consideration because of its lower computational cost. It is worth noting that small deformation simulations provide the main features of the plastic strain field maps. This has important consequences for practical implications in terms of computational efficiency for applications to in industrial components like computations of single crystal turbine blades.
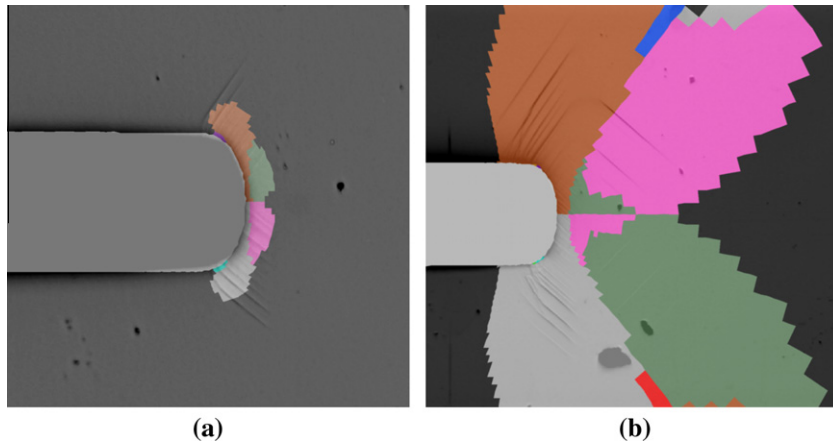
Fig. 13. Superimposed images of experiments and CPFEA results for orientation B (see Table 2 for specimen dimensions). (a) At a load of 1705 N and (b) at a load of 3510 N.
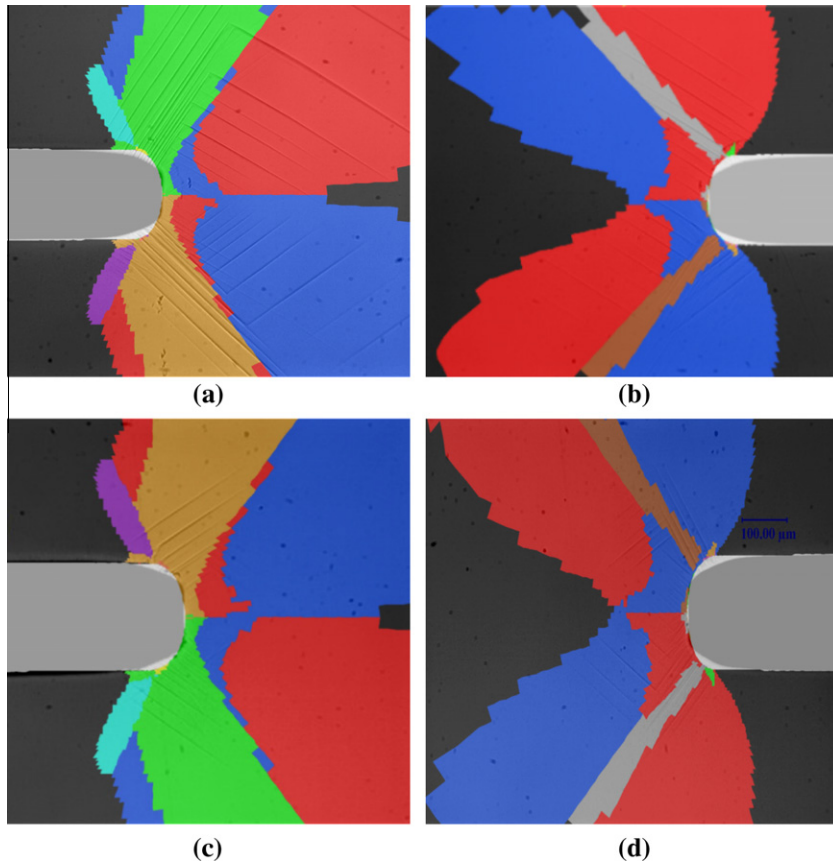

Fig. 14. Superimposed experimental slip line fields and numerical dominant slip domains for orientation C results at a load of 3486 N (see Table 2 for specimen dimensions). (a) Front face, left notch (b) Front face, right notch (c) Back face, right notch (d) Back face, left notch.

The finite deformation crystal plasticity model also provides the lattice rotation fields. This is useful information since it can be directly compared to EBSD measurements. Fig. 18 shows the lattice rotation angles for orientations A and C at 4037 N and 3474 N respectively. The (positive) rotation angle – $|\phi|$ – (in radians) is plotted in these maps. For the intermediate load in the specimen C, lattice rotation values up to 3.5° are found. At the higher load considered in specimen A, lattice rotation
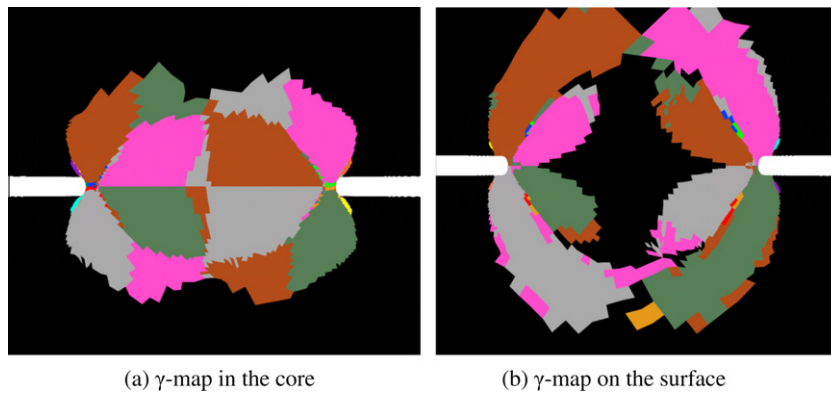
(a) γ-map in the core   (b) γ-map on the surface

Fig. 15. Fields observed at a load of 4039 N for orientation B at the specimen midplane and surface. The maps are completely different, thus indicating a strong variation in the slip fields along the thickness of the specimen (see Table 2 for specimen dimensions).
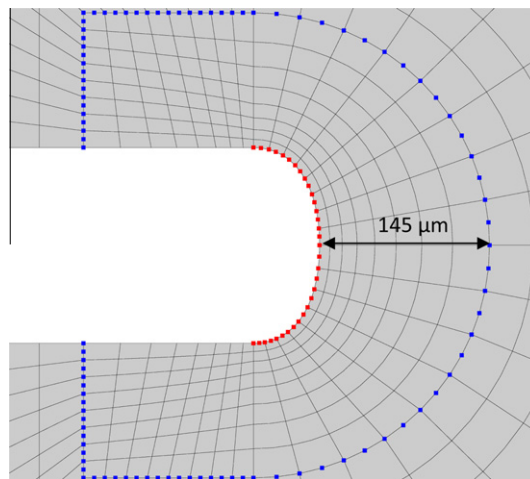

145 µm

Fig. 16. Points on the mesh used to generate the plots in Fig. 17. The blue points denote the data set away from notch tip and the red points denote the data set at the notch tip.

values of 18° are seen at certain locations. For similar loads, we find higher values of lattice rotations in sample A, which can be related to the fact that this secondary orientation is associated with more plastic strain than the other ones.

5. Discussion

The previous results are now discussed along the lines of a comparison between predictions based on AE and those based on CPFEA simulations.

5.1. Comparison of anisotropic elasticity and crystal plasticity

Three-dimensional computations of the single crystal samples based on cubic elastic symmetry (Lekhnitskii, 1963) provide information on possible subsequent slip activity if the results are post-processed to evaluate the RSS on the slip systems. Such simulations have been performed for the samples considered in the present work by Arakere et al. (2009). The elastic properties of FCC crystals exhibit cubic symmetry and can be described by three independent elastic constants which are defined by either the elastic compliance values (S_{11}, S_{12}, S_{44}), the elastic stiffness values (C_{11}, C_{12}, C_{44}), or the elastic modulus (E), shear modulus (G) and Poisson's ratio (v). The anisotropic elastic constants used are listed in Arakere et al. (2009). A 3D linear elastic anisotropic FE model with a refined mesh near the notch, using commercial ANSYS Finite element software (version 8.1), was used for computing stress fields. The component stresses at the FE nodal locations were transformed into 12 RSS components (τ^1–τ^{12}) (Table 1). These RSS values were plotted as a function of radial and angular position about the notch surface and through the thickness and were used to generate polar plots that depict the evolution of activated slip systems as a function of load. The yielding of single crystals is usually evaluated by Schmid's law, which states that plasticity
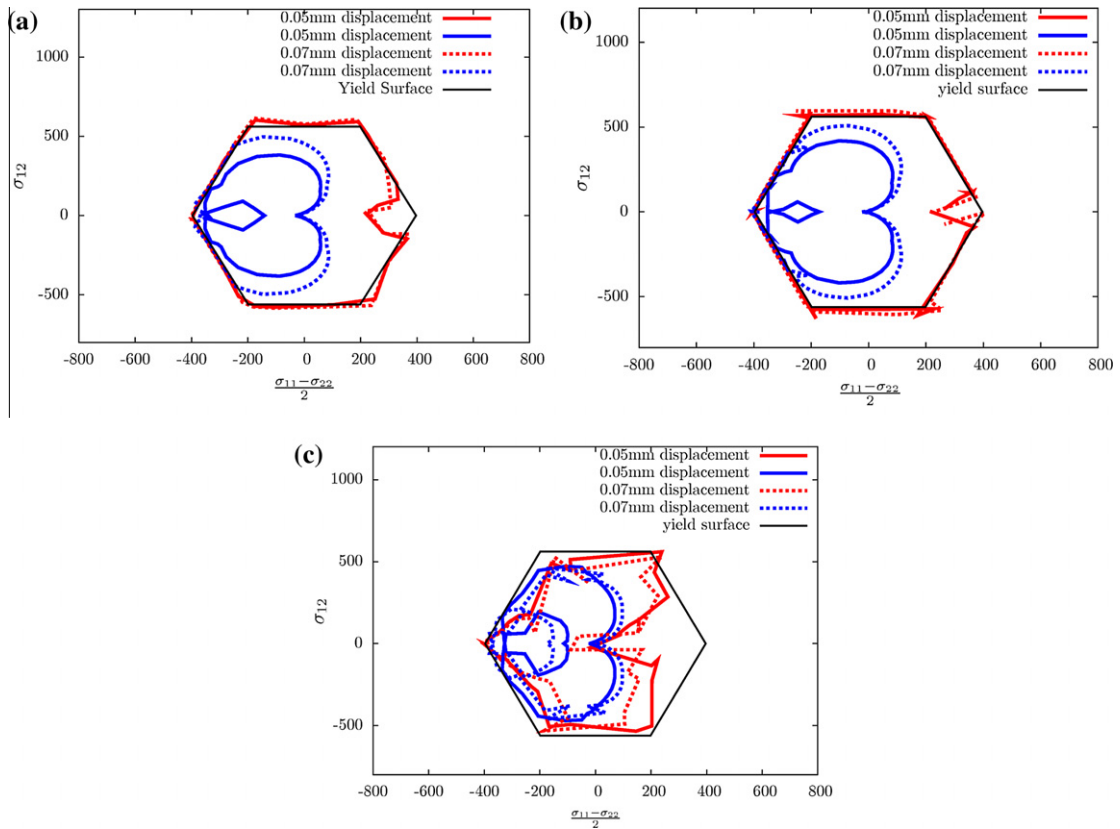
Fig. 17. Stress state plots for orientation A at different loads. The red lines represent the stress state along the notch-tip; the blue lines represent the stress state at a distance of 145 μm from the notch tip. (a) Stress state plot in a 2D specimen (plane strain simulation). (b) Stress state plot at the core of a 3D specimen. (c) Stress state plot at the free surface of a 3D specimen.

in single crystals takes place when the shear stress resolved on a slip plane and in a slip direction reaches a critical value that is independent of the loading direction. At a given (r, θ) location near the notch the slip systems that experience *initially* the highest RSS were identified and defined as "*dominant slip systems*" and were found to be the activated slip systems observed experimentally on the specimen surface. It was noticed that when plasticity was initiated in a slip system at a given (r, θ), it persisted at higher load levels, i.e. no other slip system became activated at that point except at very large loads. This observation implies that as soon as plasticity is initiated the rate of increase in resolved shear stresses on the other slip systems will be reduced significantly. The persistence of slip can partially be attributed to the softening effect due to γ'-particle shearing in the superalloy studied here (Ebrahimi et al., 2006; Westbrook, 2005). Therefore, for each point (r, θ) only one dominant slip system can be identified. Clearly, the elastic solution cannot account for nonlinear effects due to plasticity. The high CRSS of these superalloys results in high elastic strains at yield. Therefore it is possible that higher elastic strains will create larger incompatibilities among the different slip systems. However, the evolution of the "dominant slip systems" as evaluated by this work is independent of the value of CRSS. This simple approach is quite effective at identifying which slip system is activated initially at a given (r, θ), and because of persistence of activated slip systems in the superalloy used, we were able to predict slip evolution quite well at higher loads also.

Satisfying agreement was found in Arakere et al. (2009) when comparing the zones of dominant RSS to the observed slip bands. To compare CPFEA and AE simulations, the plastic zones were studied at three main load levels. Around the smaller load of 1705 N in specimen B, the extent of the plastic zone is found to be comparable with the geometric length '*a*', as defined in Table 2. For an intermediate load of about 3500 N, we find that the plastic zone size is about 2b for orientations B and C and about 4b for orientation A. At the large load levels, i.e. around 4039 N, the plastic zone size becomes comparable with the specimen thickness for all three orientations. The departure of the elastic prediction from the crystal plasticity results was mainly observed in the latter case. At higher loads, it appears that the AE simulations predict the persistent growth of initially activated slip systems even in the near notch zones for orientation A. It is observed from the Fig. 19 that AE simulations predict persistent growth of certain activated slip systems at higher loads, for example the growth of τ^6 with increasing load. But, in comparison, CPFEA seems to capture some sort of a competition between the slip systems wherein the zone in which γ^5 is dominant is taken over by the dominance of γ^4 at a higher load. This effect does not seem to be represented by the AE simulations.
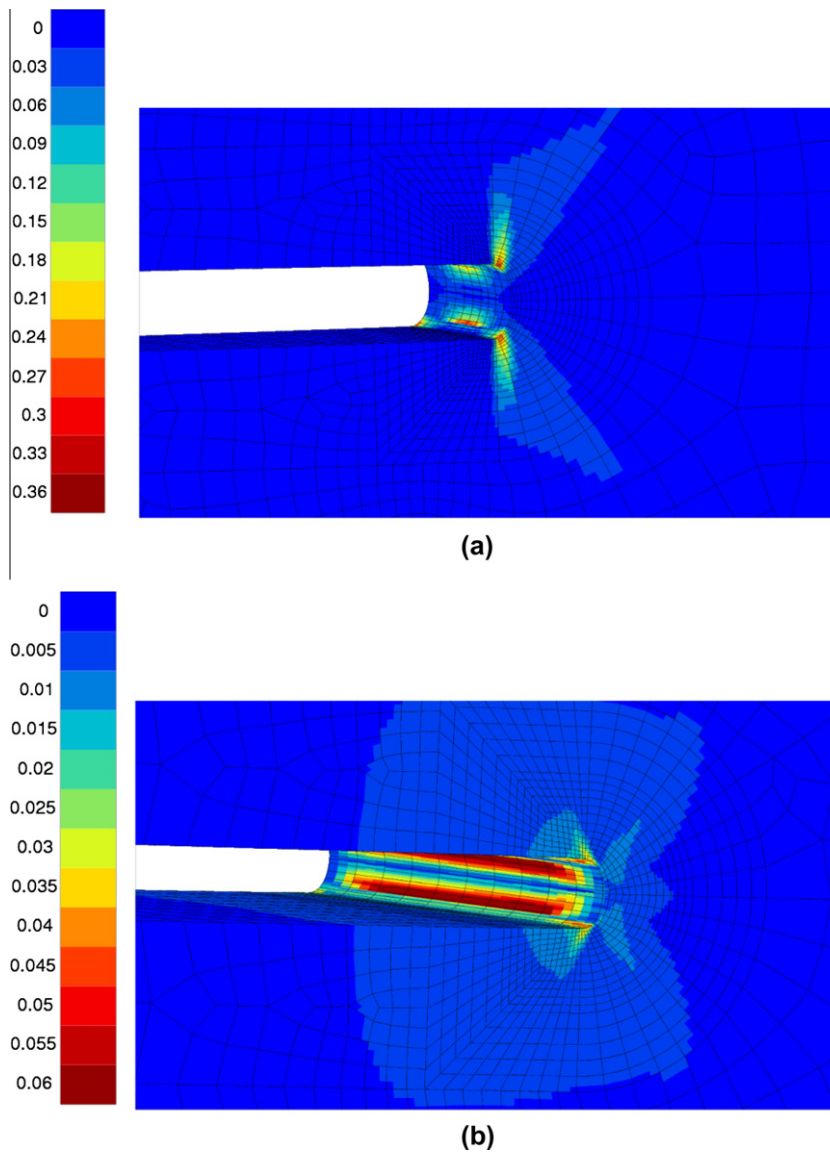
Fig. 18. Lattice rotations in radians (see Table 2 for specimen dimensions). (a) Orientation A at 4037 N. (b) Orientation C at 3474 N.

5.2. Interpretation and discussion of the γ-maps

The analysis of the dominant slip system maps raises the question of the existence of multiple slip inside each domain. However, the CPFEA results can also be used to predict secondary slip systems, i.e. the existence of a second activated slip system with less intensity, in some domains.

5.2.1. γ-map predictions and multiple dominant slip systems

It can be noted from the Figs. 15(b) and 19(c) for example, that no negative value appears, which means we systematically find one single dominant slip system in each domain even for the highly symmetric orientations A and B. One reason for this breaking of symmetry lies in the fact that we look at free surfaces, which operates on a selection of slip systems to fulfil the condition of vanishing traction at the surface. On the other hand, a close look at the specimen dimensions presented in Table 2 indicates that the specimens are not completely symmetric. These slight differences are unavoidable from an experimental perspective. However, even this slight asymmetry in the test specimens can result in a preferential selection of slip systems in the notch region.

It should be emphasised here again that the term multiple dominant slip systems refers to the cases where multiple slip systems take the same values of highest plastic slip due to several simultaneously active slip systems. This is quite different
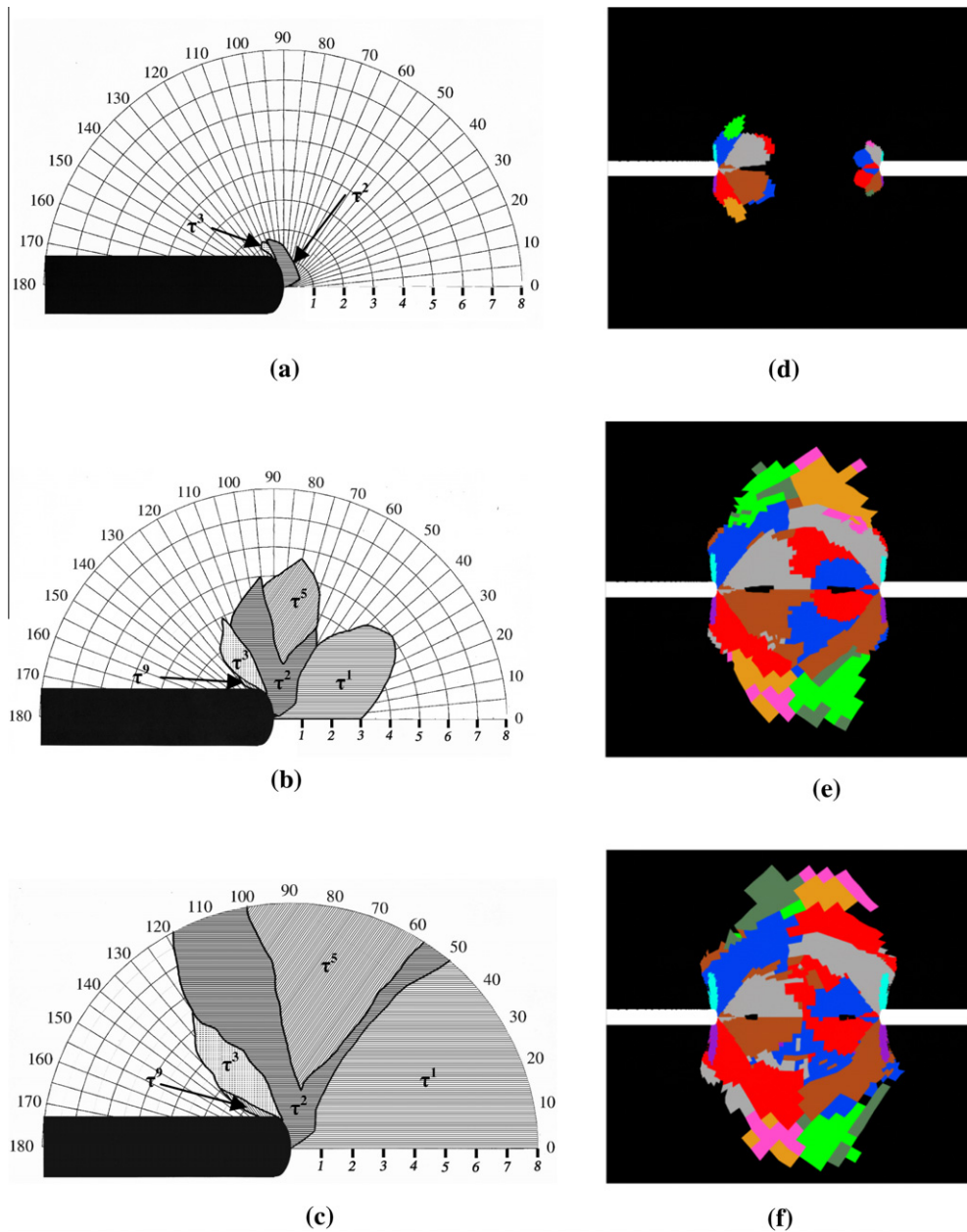
Fig. 19. (a)–(c) Comparison of orientation A fields at different loads (cf. [22]); (d)–(f) CPFEA simulation results for orientation A at 3448 N, 4037 N, 4148 N, respectively.

from multi-slip which refers to several simultaneously active slip systems with different amounts of slip. The latter cannot be distinguished in experiments.

5.2.2. Dominant and secondary slip systems

As was mentioned in the earlier sections, the γ-maps predict the lines observed on the experimental specimens with acceptable accuracy. The visibility of the slip lines at the surface of the specimen depends on the Burgers vector's component perpendicular to the z-axis. The visibility of the slip systems on the surface is described in Table 6 in terms of a *visibility index*. The "Visibility Index" here is defined as the absolute value of the scalar product between the normalised vector normal to the free surface (as indicated for the different orientations in Fig. 1) and the normalised slip direction of the slip system being considered (as defined in Table 1).

Table 6
Visibility Indices of the various slip systems on the surface of different orientations. 0 indicates that slip lines will not be visible on the surface.

Slip system number	Orientation A	Orientation B	Orientation C
1	0.5	0.707	0.223
2	0.5	0.0	0.670
3	0.0	0.707	0.447
4	0.5	0.707	0.223
5	0.5	0.0	0.670
6	1.0	0.707	0.894
7	0.5	0.0	0.670
8	1.0	0.707	0.894
9	0.5	0.707	0.223
10	0.0	0.707	0.447
11	0.5	0.707	0.223
12	0.5	0.0	0.670

In the table, a visibility index of 0 indicates that the slip/displacement component is perpendicular to the z-axis and hence does not create a slip step on the surface. Also, a greater value of the visibility index indicates a more prominent slip band.

Taking into consideration the values given in Table 6 and comparing them to the slip lines in the Fig. 12(b), it is observed that the slip systems predicted by the CPFEA simulations, i.e. the slip systems numbered 2, 5, 7 and 12 have a visibility index of 0.670. The only other slip system which has a higher visibility index of 0.894 is the slip system 8. But since the slip lines seem to be of similar prominence, it can be concluded that the γ-maps predicted by the CPFEA are accurate. Making a closer observation of the results in the area where multiple slip lines are seen (encircled area in Fig. 12(b)), the γ-map predicts a small amount of slip system 12. Among the slip systems 10, 11 and 12 (all of which have a visibility > 0) the slip system 12 has maximum amplitude of 0.003. This is however much smaller than the magnitude of slip system 7 which indicates a slip of 0.11 (0.003 and 0.11 are absolute values of the plastic strain variable at the time step obtained from the program for the slip system under consideration). Thus, the faint appearance of multiple slip lines can be explained satisfactorily by combining γ-maps with the plastic slips of individual systems.

As a further example, a similar analysis can be carried out with the orientation B (Fig. 12(a)) and the visibility values for orientation B. The slip lines observed are the ones with equal absolute visibility values. These observations further support the validity of using the γ-maps coupled with CPFEA as a means to predict the evolution of plastic slip in NBSX materials.

5.2.3. Evidence of kink shear banding

The simulation results of Fig. 19(e) and (f) predict the existence of two narrow vertical bands below and above the notch (cyan and violet colour in the pictures). One main slip system is dominant in each of these bands: $(111)[\bar{1}10]$ and $(11\bar{1})[\bar{1}10]$ respectively (systems 3 and 10), at the free surface. *The deformation bands are therefore perpendicular to the slip direction and hence must be interpreted as kink shear bands.* This is confirmed by the lattice rotation map obtained from the large strain crystal plasticity simulation of Fig. 18(a) that indicates lattice rotations close to 18° at some locations in these kink bands. *Lattice rotation in a narrow band is a characteristic feature of kink banding in crystals.* This fact has been used for experimental identification of kink bands at crack tips in single crystals (Kysar and Briant, 2002; Flouriot et al., 2003; Patil et al., 2009). The orientation of the aluminium single crystal studied in Patil et al. (2009) is the same as orientation A. The experimental observations of these authors confirm the existence of kink bands for this orientation. In our case, we have no EBSD maps available but the observation of the horizontal slip traces of Fig. 2(b) is in agreement with the numerical prediction and strongly supports the physical existence of such kink bands. It is remarkable that the solution for the crack tip field in a single crystal pointed out by Rice (1987) yields information close to what a full elastoplastic finite element analysis predicts at a crack tip but also, to some extent, at a notch. In contrast, Drugan's effort to eliminate kink bands from the solution does not seem to be in accordance with physical observations (Drugan, 2001).

6. Conclusions

The work presented was aimed at comparing the use of AE and CPFEA simulations and their respective suitability in predicting plastic slip evolution in NBSX materials. The simulations were carried out and compared against experimental images of slip line activity for double-notched specimens under tension. Post-processing procedures to generate γ-maps were introduced for the CPFEA results. Generally, a good agreement was reached between experiment and simulation for the three considered notch orientations. The results show strong differences in the plastic zone shapes and sizes for the three secondary orientations even though the loading curves for the three orientations are very close. This may have consequences on the subsequent crack initiation and propagation under monotonic or cyclic loading. The FE simulations also reveal the strong differences between the plastic strain fields at the core of the specimen and at the free surface. While this particular aspect was known in the case of cracks, it had not been investigated for notched specimens. The present study indicates the need for extensive non-destructive testing (e.g. acoustic testing) of turbine blades in service. AE simulations combined with the use of

the Schmid law as a post-processing definitively provide the correct prediction of slip system activity at the early stages of loading. Differences in the slip evolution were observed at subsequent loading stages due to nonlinear effects.

Continuum crystal plasticity simulations predict both intense slip and kink shear bands at notches and crack tips although the physical mechanisms are quite different. A limited number of dislocation sources are sufficient for the development of an intense slip band whereas many sources in parallel planes must cooperate for the formation of a kink band. This has been discussed for instance in Forest et al. (2001) especially in the context of strain gradient plasticity models, on the one hand, and of discrete dislocation dynamics simulations, on the other. It is not surprising that macroscopic kink bands can form as in the present specimen A due to the sufficiently high initial dislocation density in the nickel-base superalloy. Kink banding may be more difficult at smaller scales under confined plasticity conditions or when dislocation sources are scarce.

The comparison between FE and experimental results should be extended to other indicators of plastic slip activity, like lattice rotation which can be followed by means of EBSD field measurements close to notch, as done for wedges and cracks in (Flouriot et al., 2003; Kysar and Briant, 2002). The next step would be to consider strain field measurements by means of grids or image correlation techniques. The merit of these two techniques is that it allows for truly quantitative comparison between experiment and simulation.

Similar work should be conducted for tests at high temperature due to the use of material in turbine blades. Two-dimensional finite element simulations already exist in Marchal et al. (2006). Monotonic tests were performed on notched specimens at high temperature by Wen and Yue (2007).

The study of slip line activity at notches and crack tips is of the utmost importance to understand the subsequent mechanisms of crack propagation, that may be responsible for crack propagation on (1 1 1) planes, thus leading to complex crack paths. FE simulations of crack propagation in NBSX already exist, at least in 2D, that take into account the crystallographic nature of the active mechanisms (Bouvard et al., 2009; Aslan and Forest, 2009; Aslan et al., in press).

Acknowledgements

References

Arakere, N.K., Siddiqui, S., Ebrahimi, F., 2009. Evolution of plasticity in notched Ni-base superalloy single crystals. International Journal of Solids and Structures 46, 3027–3044.

Arakere, N.K., Swanson, G.R., 2001. Analysis of fretting stresses in single crystal Ni-base turbine blade attachment regions. ASME Journal of Tribology 123, 413–423.

Arakere, N.K., Swanson, G.R., 2002. Effect of crystal orientation on fatigue failure of single crystal nickel base turbine blade superalloys. ASME Journal of Gas Turbines and Power 124, 161–176.

Arakere, N.K., Siddiqui, S., Magnan, S., Ebrahimi, F., Forero, L., 2005. Investigation of three dimensional stress fields and slip systems for fcc single-crystal superalloy notched specimens. ASME Journal of Gas Turbines and Power 127 (3), 629–637.

Aslan, O., Quilici, S., Forest, S., in press. Numerical modeling of fatigue crack growth in single crystals based on microdamage theory. International Journal of Damage Mechanics.

Aslan, O., Forest, S., 2009. Crack growth modelling in single crystals based on higher order continua. Computational Materials Science 45, 756–761.

Borg, U., Niordson, C.F., Kysar, J.W., 2008. Size effects on void growth in single crystals with distributed voids. International Journal of Plasticity 24, 688–701.

Bouvard, J.L., Chaboche, J.L., Feyel, F., Gallerneau, G., 2009. A cohesive zone model for fatigue and creep-fatigue crack growth in single crystal superalloys. International Journal of Fatigue 31, 868–879.

Crone, W.C., Shield, T.W., 2001. Experimental study of the deformation near a notch tip in copper and copper-beryllium single crystals. Journal of the Mechanics and Physics of Solids 49, 2819–2838.

Crone, W.C., Shield, T.W., Creuziger, A., Henneman, B., 2004. Orientation dependence of the plastic slip near notches in ductile FCC single crystals. Journal of the Mechanics and Physics of Solids 52, 85–112.

Cuitiño, A., Ortiz, M., 1992. Three-dimensional crack tip fields in four-point bending copper single-crystal specimens. Journal of the Mechanics and Physics of Solids 44 (6), 863–904.

Deluca, D., Annis, C., 1995. Fatigue in Single Crystal Superalloys. Office of Naval Research, FR23800.

Drugan, W.J., 2001. Asymptotic solutions for tensile crack tip fields without kink-type shear bands in elastic-ideally plastic single crystals. Journal of the Mechanics and Physics of Solids 49, 2155–2176.

Dunne, F.P.E., Wilkinson, A.J., Allen, R., 2007. Experimental and computational studies of low cycle fatigue crack nucleation in a polycrystal. International Journal of Plasticity 23, 273–295.

Ebrahimi, F., Westbrooke, E., 2008. Effect of HIP'ping on deformation anisotropy in a single crystal Ni-based superalloy. Acta Materialia 56, 4349–4357.

Ebrahimi, F., Feroro, L., Siddiqui, S., Arakere, N.K., 2006. Effect of notch orientation on the evolution of plasticity in superalloy single crystals. Journal of Materials Science and Engineering A 426, 214–220.

Flouriot, S., Forest, S., Cailletaud, G., Koster, A., Remy, L., Burgardt, B., Gros, V., Mosset, S., Delautre, J., 2003. Strain localization at the crack tip in single crystal CT specimens under monotonous loading: 3d finite element analysis and application to nickel-based superalloys. International Journal of Fracture 124, 43–77.

Forest, S., 1997. Strain localization phenomena in generalized single crystal plasticity. Journal of the Mechanical Behavior of Materials 11, 45–50.

Forest, S., Boubidi, P., Sievert, R., 2001. Strain localization phenomena in generalized single crystal plasticity. Scripta Materialia 44 (6), 953–958.

Gan, Y.X., Kysar, J.W., Morse, T.L., 2006. Cylindrical void in a rigid-ideally plastic single crystal II: experiments and simulations. International Journal of Plasticity 22, 39–72.

Gell, M., Duhl, D.N., 1986. The Development of Single Crystal Superalloy Turbine Blades, Processing and Properties of Advanced High Temperature Materials. ASM, Metals Park, OH, p. 41.

Groh, S., Marin, E.B., Horstemeyer, M.F., Zbib, H.M., 2009. Multiscale modeling of the plasticity in an aluminum single crystal. International Journal of Plasticity 25, 1456–1473.

Horstemeyer, M.F., Bammann, D.J., 2010. Historical review of the internal state variable theory for inelasticity. International Journal of Plasticity 26, 1310–1334.

Hou, N.X., Gou, W.X., Wen, Z.X., Yue, Z.F., 2008. The influence of crystal orientations on fatigue life of single crystal cooled turbine blade. Materials Science and Engineering A 492, 413–418.

Kysar, J.W., Briant, C., 2002. Crack tip deformation fields in ductile single crystals. Acta Materialia 50 (9), 1367–1380.

Kysar, J.W., Gan, Y.X., Mendez-Arzuza, G., 2005. Cylindrical void in a rigid-ideally plastic single crystal. Part I: Anisotropic slip line theory solution for face-centered cubic crystals. International Journal of Plasticity 21, 1481–1520.

Kysar, J.W., Gan, Y.X., Morse, T.L., Chen, X., Jones, M.E., 2007. High strain gradient plasticity associated with wedge indentation into face-centered cubic single crystals: geometrically necessary dislocation densities. Journal of the Mechanics and Physics of Solids 55, 1554–1573.

Lekhnitskii, S.G., 1963. Theory of Elasticity of an Anisotropic Elastic Body. Holden-Day, Inc., San Francisco, pp. 1–40.

Magnan, S., 2002. Three-Dimensional Stress Fields and Slip Systems in Single Crystal Superalloy Notched Specimens. M.S. Thesis, Department of Mechanical & Aerospace Engineering, University of Florida, Gainesville, FL.

Mandel, J., 1973. Equations constitutives et directeurs dans les mileux plastiques et viscoplastiques. International Journal of Solids and Structures 9, 725–740.

Marchal, N., Flouriot, S., Forest, S., Remy, L., 2006. Crack-tip stress–strain fields in single crystal nickel-base superalloys at high temperature under cyclic loading. Computational Materials Science 37, 42–50.

Milligan, W.W., Antolovich, S.D., 1987. Yielding and deformation behaviour of the single crystal superalloy PWA 1480. Metall. Trans. 18A, 85.

Mohan, R., Ortiz, M., Shih, C., 1992. An analysis of cracks in ductile single crystals—II. Mode I loading. Journal of the Mechanics and Physics of Solids 40 (2), 315–337.

Nalla, R.K., Campbell, J.P., Ritchie, R.O., 2002. International Journal of Fatigue 24, 1047.

Narasimhan, R., Subramanya, H.Y., Patil, S.D., Tandaiya, P., Ramamurty, U., 2009. Stationary crack tip fields in elasticplastic solids: an overview of recent numerical simulations. Journal of Physics D: Applied Physics 42 (21).

Nouailhas, D., Culie, J.P., Cailletaud, G., Meric, L., 1995. Finite-element analysis of the stress–strain behavior of single-crystal tubes. European Journal of Mechanics A: Solids 14, 137–154.

Patil, S.D., Narasimhan, R., Mishra, R.K., 2008a. A numerical study of crack tip constraint in ductile single crystals. Journal of Mechanics and Physics of Solids 56, 2265–2286.

Patil, S.D., Biswas, R.N.P., Mishra, R.K., 2008b. Crack tip fields in a single edge notched aluminum single crystal specimen. Journal of Engineering Materials and Technology 130, 1–11.

Patil, S.D., Narasimhan, R., Mishra, R.K., 2009. Observation of kink shear bands in an aluminium single crystal fracture specimen. Scripta Materialia 61, 465–468.

Rice, J.R., 1987. Tensile crack tip fields in elastic-ideally plastic crystals. Mechanics of Materials 6, 317–335.

Rice, J.R., Saeedvafa, M., 1988. Crack tip singular fields in ductile single crystals with Taylor power-law hardening, I: anti-plane Shear. Journal of the Mechanics and Physics of Solids 36, 189–214.

Rice, J.R., Hawk, D., Asaro, R., 1990. Crack tip fields in ductile single crystals. International Journal of Fracture 42, 301–321.

Rossiter, J., Brahme, A., Simha, M.H., Inla, K., Mishra, R., 2010. A new crystal plasticity scheme for explicit time integration codes to simulate deformation in 3D microstructures: effects of strain path, strain rate and thermal softening on localized deformation in the aluminum alloy 5754 during simple shear. International Journal of Plasticity 26, 1702–1725.

Saeedvafa, M., Rice, J.R., 1989. Crack tip singular fields in ductile crystals with Taylor power-law hardening II: plane-strain. Journal of the Mechanics and Physics of Solids 37, 673–691.

Schulson, E.M., Xu, Y., 1997. Notch-tip deformation of Ni_3Al single crystals. MRS Proceedings 460, 555–560.

Shield, T.W., 1996. Experimental study of the plastic strain fields near a notch tip in a copper single crystal during loading. Acta Materialia 44, 1547–1561.

Shield, T.W., Kim, K.S., 1994. Experimental measurement of the near tip strain field in an iron-silicon single crystal. Journal of the Mechanics and Physics of Solids 42, 845–873.

Siddiqui, S.A., 2006. Evolution of plasticity (slip) in notched single crystal superalloy specimens. Ph.D. Dissertation, Department of Mechanical & Aerospace Engineering, University of Florida, Gainesville, FL.

Teodosiu, C., 1997. Large plastic deformation of crystalline aggregates. CISM Courses and Lectures No. 376, Udine, Springer-Verlag, Berlin.

VerSnyder, F.L., Guard, R.W., 1960. Directional grain structure for high temperature strength. Transactions of the American Society of Metals 52, 485.

Wen, Z.X., Yue, Z.F., 2007. Fracture behaviour of the compact tension specimens of nickel-based single crystal superalloys at high temperatures. Materials Science and Engineering A 456, 189–201.

Westbrook, E.F., 2005. Effect of crystallographic orientation on plastic deformation of single crystal nickel-base superalloys, Ph.D. Dissertation, University of Florida.

Zamiri, A.R., Pourboghrat, F., 2010. A novel yield function for single crystals based on combined constraints optimization. International Journal of Plasticity 26, 731–746.